

Bioactive Functionalized Monolayer Graphene for High-Resolution Cryo-Electron Microscopy

Nan Liu,^{†,‡,∇} Jincan Zhang,^{§,||,∇} Yanan Chen,^{*,†,∇} Chuan Liu,[†] Xing Zhang,[†] Kui Xu,^{†,‡} Jie Wen,[†] Zhipu Luo,[†] Shulin Chen,[⊥] Peng Gao,^{⊥,#} Kaicheng Jia,[§] Zhongfan Liu,[§] Hailin Peng,^{*,§,||} and Hong-Wei Wang^{*,†,‡,Ⓛ}

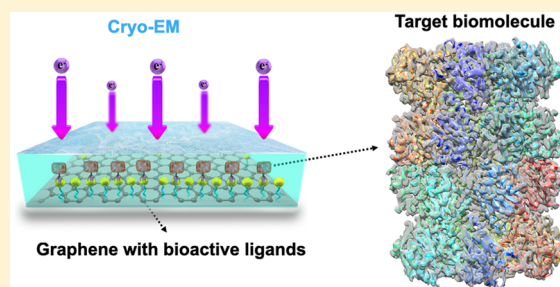
[†]Ministry of Education Key Laboratory of Protein Sciences, Beijing Advanced Innovation Center for Structural Biology, School of Life Sciences and [‡]Tsinghua-Peking Joint Center for Life Sciences, Tsinghua University, Beijing 100084, China

[§]Center for Nanochemistry, Beijing Science and Engineering Center for Nanocarbons, Beijing National Laboratory for Molecular Sciences, College of Chemistry and Molecular Engineering, ^{||}Academy for Advanced Interdisciplinary Studies, and [⊥]International Center for Quantum Materials, and Electron Microscopy Laboratory, School of Physics, Peking University, Beijing 100871, China

[#]Collaborative Innovation Center of Quantum Matter, Beijing 100871, China

Supporting Information

ABSTRACT: Single-particle cryo-electron microscopy (cryo-EM) has become one of the most essential tools to understand biological mechanisms at molecular level. A major bottleneck in cryo-EM technique is the preparation of good specimens that embed biological macromolecules in a thin layer of vitreous ice. In the canonical cryo-EM specimen preparation method, biological macromolecules tend to be adsorbed to the air–water interface, causing partial denaturation and/or preferential orientations. In this work, we have designed and produced a new type of cryo-EM grids using bioactive-ligand functionalized single-crystalline monolayer graphene membranes as supporting films. The functionalized graphene membrane (FGM) grids exhibit specific binding affinity to histidine (His)-tagged proteins and complexes. In cryo-EM, the FGM grids generate relatively low background for imaging and selectively anchor 20S proteasomes to the supporting film surface, enabling near-atomic-resolution 3D reconstruction of the complex. We envision that the FGM grids could benefit single particle cryo-EM specimen preparation with high reproducibility and robustness, therefore enhancing the efficiency and throughput of high-resolution cryo-EM structural determination.



INTRODUCTION

Single particle cryo-electron microscopy (cryo-EM) has become an important structural biology research method in recent years due to major technological breakthroughs in both hardware and software.^{1,2} However, cryo-EM is still far from a mature technology, and its wider development and application are limited by certain bottlenecks, one of which is the specimen preparation to freeze biological macromolecules in vitreous ice. Several novel instruments have been developed recently for vitrifying biomolecules,^{3–5} exemplified by Spotiton³ and CryoSol-Word VitroJet. These instruments, however, are less automated or uneasily controlled, and tend to causing biomolecules touching the air–water interface. Thus, the current extensively applied method for cryo-EM specimen preparation has largely remained the same as invented in 1980s,⁶ implemented by commercial devices, like Thermo Fisher Scientific Vitrobot, Gatan CP3, or Leica GP. In the most popular practice, a small volume of liquid solution containing macromolecules is applied to a metal grid covered with a thin layer of holey amorphous carbon film that is glow-discharged to be hydrophilic; the solution is blotted with a

piece of filter paper to form a very thin layer of liquid (thickness of tens of nanometers) spanning over the holes on the carbon film. The grid is plunged into liquid ethane cooled at ~100 K temperature to flash freeze the liquid layer into unstructured ice embedding macromolecules.

The holey amorphous carbon membrane on a metal TEM grid is commonly used in the conventional cryo-EM specimen preparation. The holey carbon grid is relatively easy to fabricate but has shortcomings that limit the producibility and robustness of cryo-EM specimen preparation. For example, the holey carbon film has uneven surface properties,^{7,8} inconsistent thickness of the hole edges, and poor electrical conductivity of the amorphous carbon frames. More severely, the air–water interface of the thin layer of solution suspended over the holes often causes the adsorption of protein molecules to it and thus leads to an adverse effect on the structural stability, particle orientation, and uniformity of distribution of the biomolecules.^{9–11} To avoid the air–water interface adsorption

Received: December 10, 2018

Published: February 6, 2019

Scheme 1. Schematic Illustration of Bioactive Ligands Functionalized Monolayer Graphene Showing Affinity Binding and Selectivity of Target Proteins for High-Resolution Cryo-EM

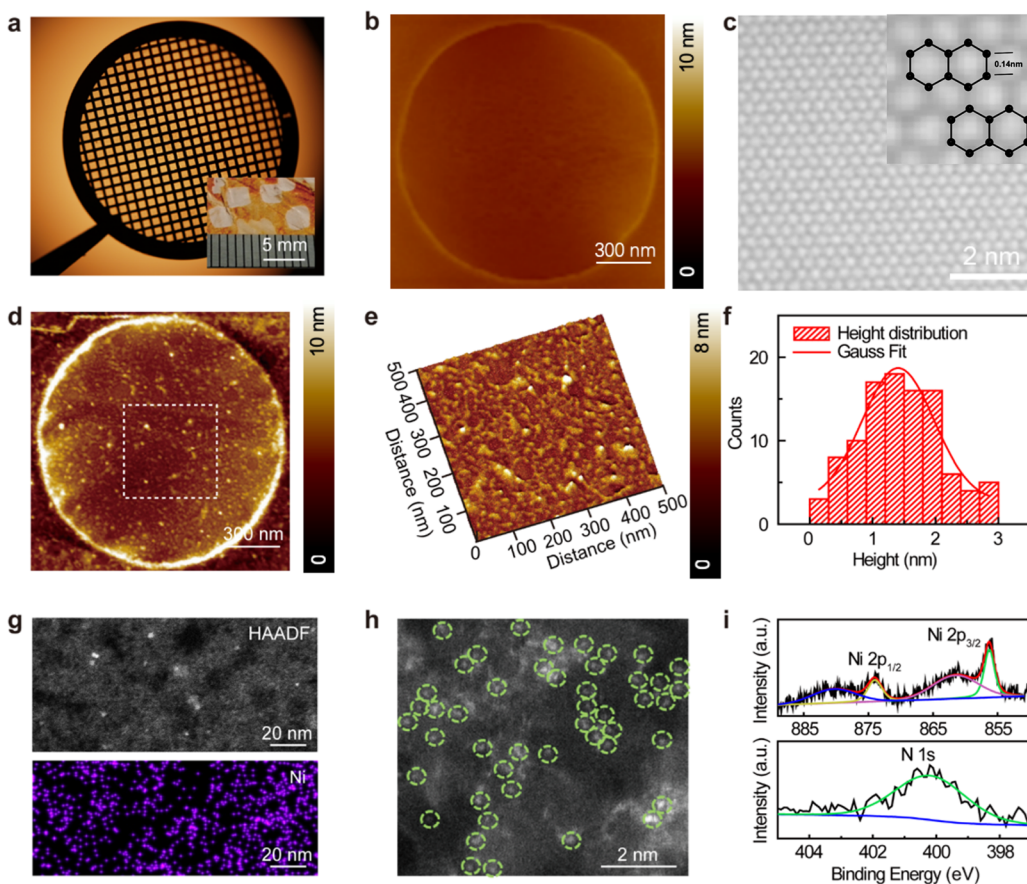
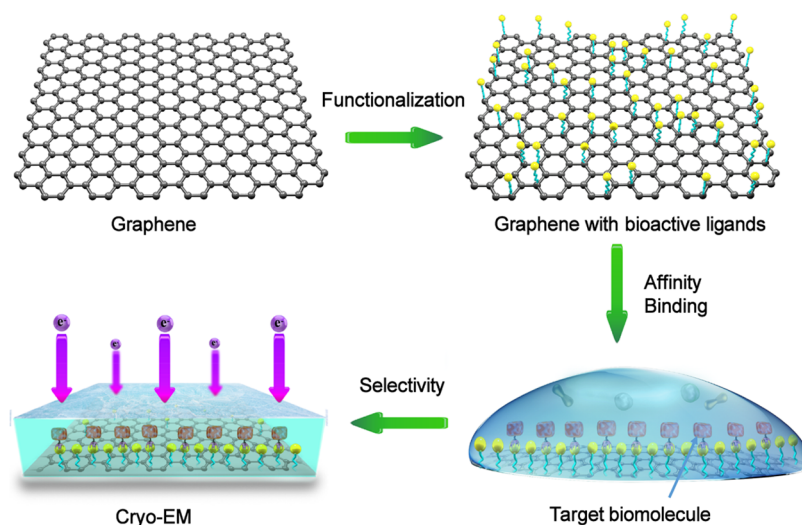


Figure 1. Characterization of nickel atoms modified suspended monolayer graphene. (a) Optical microscopy image of a TEM grid (Quantifoil) covered by the clean, suspended, single-crystal graphene membrane (GM) with subcentimeter size by a polymer-free transfer technique. Inset shows the corresponding pristine, large-area, monolayer graphene single crystals grown on the copper foil. (b) AFM characterization of the suspended GM after transferred onto Quantifoil Au frame from Cu substrate. The contrast change in scale bar next to the image represents the height. (c) High-resolution TEM image of the GM suspended on Quantifoil holey carbon, presenting a perfect honeycomb lattice. Inset: magnified TEM image of GM with carbon hexagons outlined. (d) 2D AFM image of functionalized graphene membrane (FGM). (e) Corresponding high-magnification AFM 3D image of FGM in the square region marked in (d). (f) Statistic histogram of the height distribution of the modified ligands on graphene surface. (g) STEM image of graphene membrane modified by Ni-NTA and the corresponding EDX elemental mapping of Ni, revealing a uniform distribution of nickel atoms on graphene surface. (h) High-resolution STEM image showing potential individual nickel atoms on the graphene surface, labeled by the green circles. (i) High-resolution Ni 2p, N 1s XPS spectra of Ni-NTA modified graphene, respectively.

problem, scientists often use thin layer of amorphous carbon film over the holes but have to deal with the strong background noise introduced by the carbon film. Furthermore, the poor electrical conductivity of the amorphous carbon film particularly below the liquid nitrogen temperature causes other problems such as the surface charging and radiation-induced chemical and physical damages of the specimen.^{12,13} The conventional cryo-EM specimen preparation method thus faces challenges of reproducibility, universal versatility, and homogeneity of specimen quality. As a result, large amounts of labor as well as material resources are spent on optimizing the cryo-specimen preparation step.

Faced with the current challenges, several research groups have explored new types of supporting materials to improve the quality of frozen specimens, including two-dimensional (2D) crystals of streptavidin,^{14,15} lipid monolayers,^{16,17} and double-stranded DNA scaffolds.¹⁸ However, these methods introduce large amounts of biomass into the final sample and require specific conditions to maintain the integrity of the incoming material.¹⁹ Considering the superior properties of monatomic layer graphene with excellent electrical conductivity,²⁰ thermal conductivity,²¹ chemical and temperature resistance^{22–26} and mechanical strength,²⁷ people have started to investigate graphene as a new supporting material for cryo-EM specimen preparation.²⁸ Due to the low-cost and hydrophilicity,^{29,30} graphene oxide was also explored to serve as imaging matrices for freezing hydrated biomolecules.^{31,32} Stahlberg et al. proposed the use of hydrophilic graphene as an electron microscopy support for biological specimens by graphene surface oxidation doping or noncovalent aromatic modification.^{33,34} Russo et al. reported that graphene can be used as a cryo-EM supporting film for biological specimens after low-energy hydrogen plasma treatment and that graphene can reduce the radiation-induced motion of the specimen.³⁵

Although graphene shows great potential as the supporting film for cryo-EM, it still faces a major problem for cryo-EM specimen preparation, that is, the lack of control of protein distribution within the vitreous ice sheet. Using a functionalized surface to specifically anchor macromolecules to the supporting material could potentially solve the problem of protein adsorption to the air–water interface and simultaneously enrich target macromolecules with low abundance or low expression level in heterologous systems in the cryo-EM specimen. Affinity ligands like nickel-nitrilotriacetic acid (Ni-NTA) or antibodies functionalized amorphous carbon films or graphene oxide flakes have been reported to catch protein complexes of interest.^{36–40} Nevertheless, the amorphous carbon, as mentioned before, leaves strong background noise when imaged under electron microscopy. Likewise, the graphene oxide flakes largely vary in numbers of layers on EM grid, leading to a discontinuous and uneven film with poor electrical conductivity.

In this work, we chemically modified the monolayer single-crystal graphene to link bioactive ligands to the basal plane of the graphene thus generating a functionalized graphene EM grid. We introduced biologically active ligands with negligible biomass, such as Ni-NTA, onto the suspended functionalized graphene surface for it to have specific affinity to biological molecules with His-tag (Scheme 1). We have characterized the bioactive functionalized graphene membrane (FGM) grid and found it to be a potentially general applicable supporting substrate for robust cryo-EM specimen preparation to determine structures of macromolecules at atomic resolution.

RESULTS

Preparation and Characterization of Bioactive FGM Grids. The fabrication of EM grids covered with suspended, large-area, single-crystalline monolayer graphene membrane (GM) was achieved by using a previously established method recently developed by us.⁴¹ Starting from monolayer graphene single crystals with domain size larger than 3 nm on copper foil (inset of Figure 1a), synthesized by chemical vapor deposition (CVD),⁴² we assembled the copper/graphene/holey carbon grid by adhering the graphene/copper foil onto a holey carbon grid (Quantifoil, Au frame, 300 mesh, R1.2/1.3 μm) assisted by isopropanol (IPA) solution.⁴¹ We then removed the copper foil from the assembly using the $(\text{NH}_4)_2\text{S}_2\text{O}_8$ aqueous etching solution to obtain the suspended, single-crystal graphene membrane (GM) adhered to the Quantifoil holey carbon coated gold grid (Figure 1a). The graphene supporting membrane grids exhibited high coverage ratio on the holey carbon (90% percentage on average) and clean contrast without obvious pollutants under low-magnification TEM, illustrating the successful fabrication of the suspended graphene membrane by the polymer-free transfer technique (Figure S1). We also conducted atomic force microscopy (AFM) characterization to evaluate the quality of the suspended GM on Au grid (Figures 1b and S2) and found that it exhibited high intactness and clean surface with absence of transfer-related contamination. Breakage of the graphene membrane was rarely observed over the holes. The average roughness of the suspended region of GM is smaller than 0.25 nm (Figure S2b). The high stability and integrity of the suspended GM is likely due to the high order of crystalline and large domain size (centimeter-sized) of the single-crystal monolayer graphene. Further examination of the graphene membranes on the grids under a low-voltage (80 kV) aberration-corrected TEM at high magnification verified the clean graphene surface with absence of transfer-related contamination and perfect single crystalline hexagonal lattice of monolayer graphene with the distance of 0.14 nm between carbon atoms (Figure 1c).

We functionalized the as-prepared suspended GM grids through a series of chemical reactions in order to achieve the specific functionality (details in the “Methods” section) with a biologically active ligand Ni-NTA and characterized the quality of the functionalized graphene membrane (FGM) using a set of microscopy and spectroscopy analysis. The suspended GM could bear the multiple operations during the functionalization process so well that no extra breakage of graphene membrane was introduced after the chemical modification. Compared to the unmodified suspended GM, the FGM’s surface was rougher with additional structural features (Figure 1d,e), and the surface height fluctuation was mainly distributed in a range of 1–2 nm (Figures 1f and S3). The average height of the linked ligands is much smaller than the thickness of amorphous carbon thin film (~ 5 nm) used in conventional cryo-EM, therefore potentially reducing the background noise of the TEM supporting film significantly. STEM imaging and the corresponding EDX elemental mapping of the FGM illustrated the homogeneous distribution of Ni atoms across the graphene surface, demonstrating the successful introduction of Ni-NTA onto GM (Figure 1g). High-resolution STEM of the FGM showed dispersed high contrast features likely corresponding to separated nickel atoms on the modified graphene surface (Figure 1h), and approximately every 16 hexagonal graphene

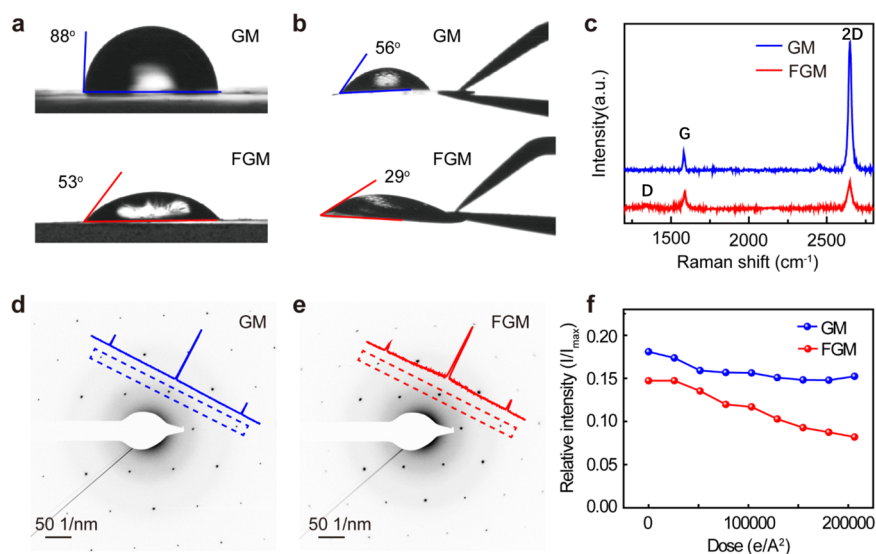


Figure 2. Characterization on hydrophilicity and strength of FGM. (a) Hydrophilicity of graphene on Cu before (top) and after (bottom) functionalization treatment, with the water contact angles (WCAs) being 88 and 53°, respectively. (b) Hydrophilicity of suspended graphene on grids before (upper) and after (down) the functionalization treatment, with WCAs being 56 and 29°, respectively. (c) Raman spectra of suspended graphene before (red) and after (blue) the functionalization treatment. D (1350 cm^{-1}), G (1580 cm^{-1}), and 2D (2690 cm^{-1}) peaks were labeled. (d, e) Selected area electron-diffraction (SAED) patterns for graphene membrane (GM) and Ni-NTA functionalized graphene membrane (FGM) after 1s exposure at a dose rate of 86 $\text{e}/\text{Å}^2/\text{s}$. The corresponding intensity of the dotted rectangular boxes was indicated. (f) Ratio of third-order integrated Bragg intensity (I) to the first-order integrated Bragg intensity (I_{max}) as a function of dose for GM and FGM, respectively.

lattices there was on average one fabricated nickel atom, which was estimated by calculating the nickel atoms number on FGM areas.

We next used X-ray photoelectron spectroscopy (XPS) to analyze the elemental composition and electronic structure of the FGM. All the XPS spectra were calibrated to the 284.0 eV binding energy of sp^2 carbon. The XPS spectra presented signals of C 1s, O 1s, N 1s, Ni 2p, and Au 2p (1s and 2p correspond to the electron configuration of the electrons within the atoms) for FGM with atomic ratios of 83.2, 13.6, 1.0, 0.8, and 1.3%, respectively (Figure S4). Among these, the spectral signal of Au came from the Quantifoil gold grid bars which support the holey carbon. The high-resolution Ni 2p spectrum revealed two prominent bands at 856.4 and 874.1 eV (Figure 1i), corresponding to Ni 2p_{3/2} and Ni 2p_{1/2}, respectively, consistent with the literature values of electron-binding energies of Ni²⁺ cations.⁴³ The characteristic peak of N 1s centered at 400.3 eV in the high-resolution N 1s spectrum can be assigned to C–NH₂ bonds, derived from NTA covalently linked to the graphene membrane (Figure 1i).

Physicochemical Properties of FGM Grids. We evaluated the hydrophilicity of the FGM grids using the water contact angle (WCA) measurement. We examined the effect of functionalization treatment on graphene's hydrophilicity on both graphene membranes grown on copper foil surface (Figure 2a) and transferred to Au grids (Figure 2b). Figure 2a showed that the WCA of graphene on copper foil decreased from 88° to 53° after the functionalization treatment (details in the "Methods" section). On the transferred Au grids, the WCA decreased from 56 to 29°, indicating high hydrophilicity after the treatment (Figure 2b).

The integrity of carbon–carbon bond in the graphene is critical for its special physical properties. We examined the Raman spectrum of the suspended GM and FGM grids. The results revealed that the intensity ratio of 2D (2690 cm^{-1}), the two-phonon band coming from the second order Raman

scattering) to G (1580 cm^{-1} , first-order Raman scattering) peaks is nearly 8 with the absence of defect peak in the suspended GM, proving the high quality of the graphene (Figure 2c). After the functionalization treatment, the shapes of G and 2D peaks of graphene were kept well, with the appearance of a negligible D peak (1350 cm^{-1} , defect-induced second-order Raman scattering, Figure 2c). The intensity ratio of D peak (1350 cm^{-1}) over that of G peak (1580 cm^{-1}) was approximately 0.19, much lower than that of graphene oxide (close to 1) synthesized by the improved Hummers method,^{22,23} indicating that modification procedures described in our work preserved the graphene lattice much better. This guaranteed the high thermal and electrical conductivity and mechanical strength of the FGM and its potential capability to reduce the electron radiation damage to specimens. We investigated the effect of electron radiation on the FGM's stability by examining the diffraction pattern change of the graphene membranes in a TEM (Figure 2d,e). The sharp peaks in the diffractogram of FGM were very similar to those of suspended GM after 1s exposure at an electron dose rate of 86 $\text{e}/\text{Å}^2/\text{s}$ accelerated at 200 kV (Figure 2d,e), demonstrating that the FGM preserves the lattice structure after Ni-NTA modification. The relative intensities of Bragg reflections for GM and FGM, defined as the ratio of the third-order integrated intensity of Bragg peaks to the first-order integrated intensity, both exhibited small decays even with a high electron radiation up to $\sim 200\,000$ $\text{e}/\text{Å}^2$ (Figure 2f). The negligible radiation damage on the grids illustrated the high stability of FGM under electron beam, which should attribute to the high electrical conductivity property of the continuous large-area crystalline graphene membrane.

Biological Binding Activity of FGM Grids. We first verified the binding capability of FGM using His-tagged red fluorescent protein (RFP) by fluorescence microscopy. We functionalized graphene membrane grown on copper foil with Ni-NTA as mentioned above and applied ~ 1 mL of His-tagged

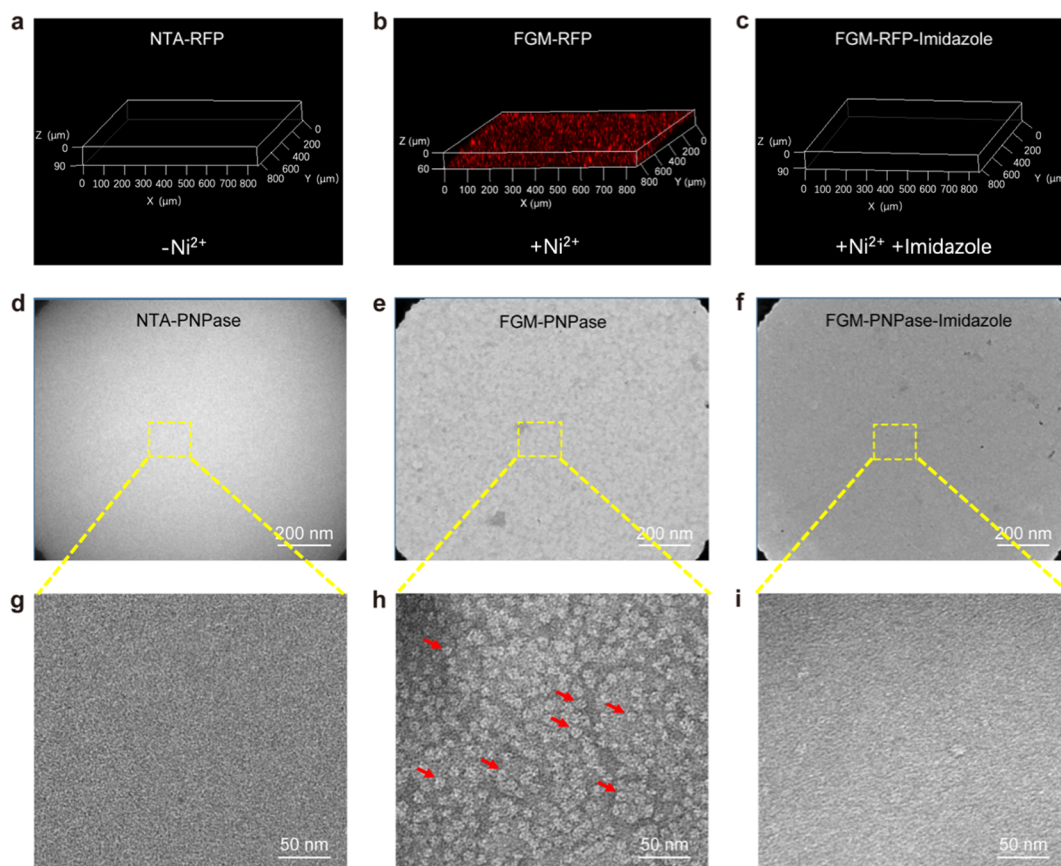


Figure 3. Characterization of binding affinity of FGM by fluorescence as well as negative-staining electron microscopy. (a) His-tagged RFP was incubated with graphene membrane treated as FGM but in the absence of Ni ion. No red signals were detected under fluorescence microscopy. (b) Red signals in high density bound to FGM with Ni ion. (c) The red signals were washed off by 300 mM imidazole buffer. (d–i) Negative-staining EM characterization of His-tagged PNPase binding affinity. (d, g) Almost no protein particle was attached to graphene membrane grids treated as FGM grids but in the absence of Ni ion. (e, h) Representative micrograph of His-tagged PNPase supported by FGM grids where the protein particles were visibly identified. Some protein particles were indicated by red arrows. (f, i) Protein particles were washed off by 300 mM imidazole buffer. (g–i) Micrographs acquired with magnification higher than that of (d–f), respectively.

RFP at a concentration of 2 mg/mL to the FGM surface. After incubation with protein solution at room temperature for 15 min, the FGM surface was washed with protein buffer and examined under fluorescence microscopy. Red fluorescent spots in high density were clearly recognized on the surface (Figure 3b), indicating the presence of His-tagged RFP. To verify that the accumulation of His-tagged RFP on the FGM surface was specific, we performed control experiments by washing the RFP-bound FGM with 300 mM imidazole and found that almost all the red signals were depleted (Figure 3c). In a parallel experiment, we intentionally omitted the Ni ions during the chemical modification step. The lack of Ni ions fully abolished the binding capability of FGM so that no RFP signal was detected on the FGM surface (Figure 3a). To test the affinity of Ni-NTA FGM grids, we used negative-staining EM to examine their binding ability to His-tagged PNPase protein (Figure S5). Agreeing with the fluorescence microscopy results, almost no protein particles were identified in the absence of Ni ions (Figure 3d,g). When the Ni ion was present during the chemical modification, the FGM grids can adsorb monodispersed protein particles with high signal-to-noise ratio (Figure 3e,h), and these attached PNPase particles disappeared after washed by 300 mM imidazole (Figure 3f,i), confirming that the His-tagged proteins were specifically bound to FGM via Ni-NTA chelation.

Application of FGM Grids for Cryo-EM Reconstruction. We further characterized the FGM grids for cryo-EM specimen preparation using a mixture solution of His-tagged 20S proteasomes and pre-60S ribosomes in a molar ratio of $\sim 1:1$. As controls, we also used amorphous carbon coated grids (Figure 4a) and NTA-functionalized GM (in the absence of Ni ion) grids (Figure 4b) to make cryo-EM specimens. The two-dimensional class averages of both 20S proteasomes and pre-60S ribosomes on the FGM grids contained more fine details than those on the amorphous carbon coated grids from roughly the same number of particle images (Figure 4c and 4a insets). To further confirm the selectivity of the FGM grids on His-tagged protein over nontagged proteins, we classified and calculated the distribution of the images of the mixed His-tagged 20S proteasomes and pre-60S ribosomes sample on the FGM grids lacking Ni ion (Figure 4b) and Ni-NTA modified FGM grids (Figure 4c) by single-particle cryo-EM analysis. Indeed, the particle ratio of His-tagged 20S proteasome to pre-60S ribosome on the Ni-NTA modified FGM grids increased by 9-fold over that of the NTA modified GM grids (Figure 4d). Clearly, there was still certain amount of nonspecific adsorption of the pre-60S ribosomes on the grids. This might be partially due to the large composition of negatively charged RNAs in the pre-60S ribosomes.

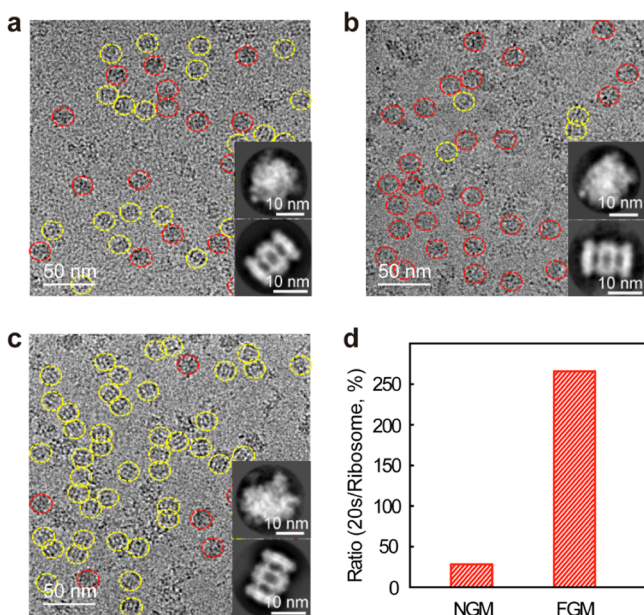


Figure 4. Application of FGM grids on cryo-EM specimen preparation. (a) Representative micrograph of proteins mixed by His-tagged 20S proteasomes (labeled by yellow circles) and pre-60S ribosomes (red circles) on amorphous carbon film. Insets were selected averaged classes generated in 2D classification by Relion, with upper one for pre-60S ribosome and lower for 20S proteasome. (b) Representative micrograph of mixed proteins on NTA FGM grids in the absence of Ni ion. Particles are labeled as in (a). Selected 2D class averages of pre-60S ribosome and 20S proteasome are shown in the inset as in (a). (c) Representative micrographs of mixed proteins on Ni-NTA modified FGM grids. Particles are labeled as in (a). Selected 2D class averages of pre-60S ribosome and 20S proteasome are shown in the inset as in (a). (d) Statistical analysis of protein proportional change. Ratio of His-tagged 20S proteasomes over ribosome was approximately 30% on NTA modified GM in the absence of Ni ion (NGM), but increased by 9-fold to 270% on Ni-NTA modified FGM.

We next performed cryo-electron tomography (cryo-ET) of His-tagged 20S proteasome on the FGM grid to further characterize the property of the cryogenic specimen (Figures S5c,d and S7). The ET data illustrated that almost all the 20S particles were adsorbed to the graphene membrane in the same layer on the FGM grid. In contrast, in the control specimens that 20S proteasomes were applied onto holey carbon grids (Quantifoil), most of the proteasome particles distributed to the upper or bottom air–water interface of the vitreous ice (Figures S5a,b and S6). The latter phenomenon was also observed and discussed by other groups.^{9,11,44} Notably, orientation of almost all the 20S proteasome particles was recognized as side (rectangle-shaped) view when supported by FGM grids (Figure S7), which was consistent with the affinity binding strategy of proteasomes containing β subunits tagged by histidine (His) residues to FGM. For particles supported by holey carbon grids, both top (ring-shaped), and side (rectangle-shaped) views of 20S proteasome could be identified at the air–water interface as well as within the vitreous ice (Figure S6), indicating that His-tagged proteasomes specifically bound to FGM by interacting with the Ni-NTA ligand on its surface. Together, these experimental results indicate that the FGM grid has the advantage to prevent targeted macromolecules from being adsorbed to the air–water interface.

In practice, we found it was more controllable to make cryo-specimens with an optimal ice thickness of 20–30 nm when utilizing FGM grids (Figures S5d and S7), and such ice thickness was considered ideal for embedding most bio-molecules without introducing extra background noise.⁹ Vitreous ice on FGM was more uniform compared to that on holey carbon grids (Figure S5a). Moreover, the estimation of CTF parameters such as defocus values of particles on FGM grids during data processing becomes more reliable because most of the protein particles are located at the same plane. In contrast, particles supported by holey carbon grids were adsorbed into the upper or bottom air–water interface, resulting in large variation in height and making data processing, especially CTF estimation, more complicated and less accurate. As a consequence, from exactly the same number (6095) of particle images, the final resolution of 3D reconstruction of 20S proteasomes on FGM was reported as 3.8 Å, much higher than that as 6.2 Å on the continuous carbon coated grids and 4.4 Å on the holey carbon coated grids (Figure S8a). The Euler angle distributions of 20S proteasome particles also show some differences. A portion of particles on continuous carbon or holey carbon has alternative views (Figure S8b) in addition to the side view. However, these alternative views were barely recognized on FGM, providing another evidence to prove that His-tagged 20S proteasomes were captured onto FGM by the specific interaction of Ni-NTA and the His-tag. Due to the D7 symmetry of the 20S proteasome, we could obtain the 3D cryo-EM reconstruction of His-tagged 20S proteasome on FGM grids at 3.8 Å resolution, which was good enough to unambiguously trace the main chain backbone of the asymmetrical α - and β -subunit and identify some bulky side chains (Figure S5e–g). The interaction interface among the subunits within the 20S proteasome can also be solved with high precision to define the molecular mechanism of the complex’s biological function. Collectively, the FGM grids exhibit specificity to capture His-tagged proteasomes and are suitable as a supporting material for cryo-EM reconstruction to near-atomic resolution.

CONCLUSION

In summary, we presented bioactive ligands functionalized graphene membrane (FGM) as a new supporting material in cryo-EM structural analysis. We showed that the FGM has little or no influence on the graphene lattice and maintains the superior properties of single crystalline monolayer graphene, thus effectively reducing the background noise in the raw cryo-EM micrographs compared to amorphous carbon films. FGM is naturally hydrophilic and more friendly to biomolecules, compared to amorphous carbon grids. Furthermore, it is capable of capturing proteins of interest, better preserving protein molecules in an environment away from the air–water interface. The FGM shows high specificity in selecting target proteins and reducing the amount of protein used for specimen preparation, therefore simplifying protein purification and improving the protein stability. These all open up new prospects of using graphene-based materials for cryo-EM. Prominent merits of FGM make it more controllable to prepare vitrified cryo-EM specimen with uniform and appropriate ice thickness and more reliable to perform data processing, especially in CTF estimation, for high-resolution cryo-EM structural determination. We anticipate that the bioactive FGM grids could make it possible to combine biomolecules purification and cryo-EM specimen preparation

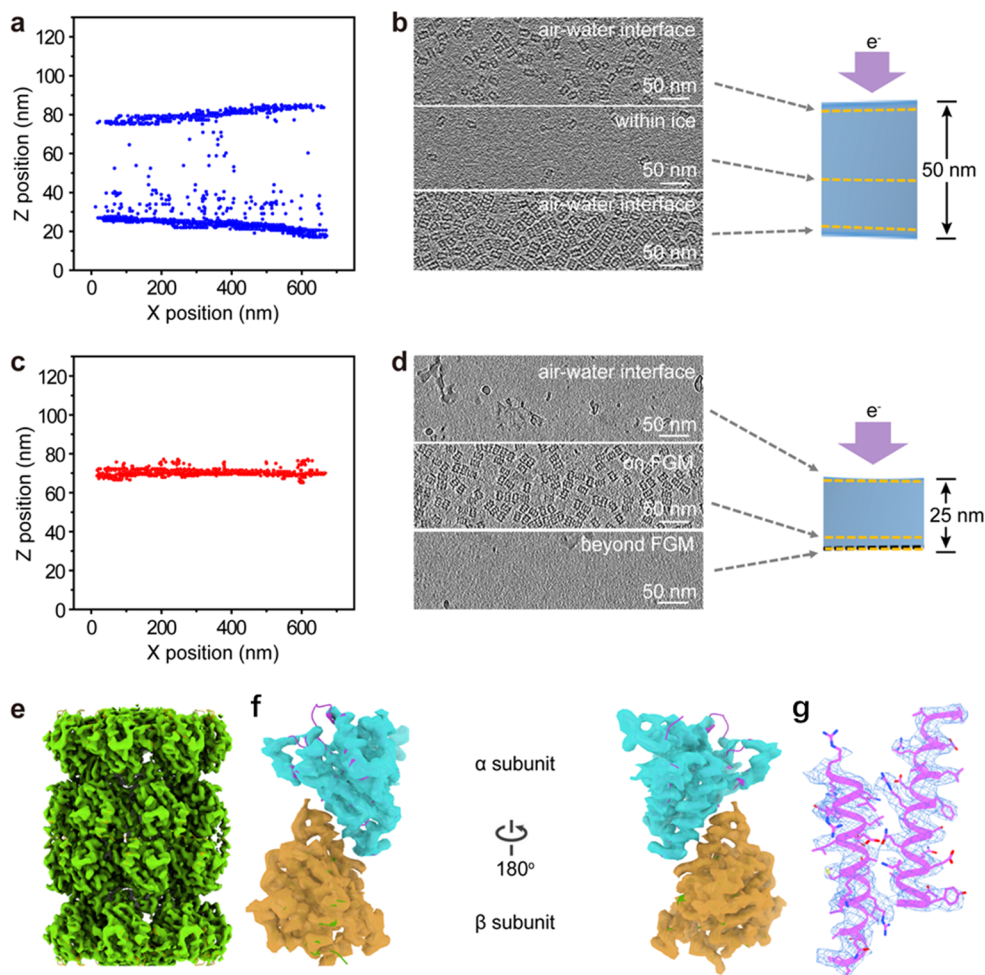


Figure 5. Cryo-EM structure determination of complexes prepared on FGM grids. (a) Localization of 20S particles in a holey carbon coated grid as revealed by cryo-ET. Each spot represents one 20S particle. (b) Three different layers through Z-axis from cryo-ET reconstruction in (a) were listed, and their relative locations were indicated by the arrows. The thickness of cryo-specimen was estimated as ~ 50 nm (Figure S6). Scale bars in these layers represented 50 nm. (c) Localization of 20S particles in an Ni-NTA FGM grid as revealed by cryo-ET. Each spot represents one 20S particle. These particles were mainly distributed at the same layer. (d) Three representative layers through Z-axis from cryo-ET reconstruction in (c) were listed, and their relative locations were indicated by the arrows. The thickness of cryo-specimen was estimated as ~ 25 nm (Figure S7). Scale bar represents 50 nm. (e) 3D reconstruction of 20S proteasome using particle images collected from the Ni-NTA FGM specimen. (f) Two different views of α - and β -subunits density extracted from the 3D reconstruction with the corresponding atomic models fitting in. (g) Interacting α -helices density (meshed) segmented from the α - and β -subunits interface fitted by the atomic model (purple ribbon, Protein Databank (PDB) code: 3J91), and densities of some bulky side chains are clearly identified.

into one step by directly locate or capture target biomolecules from cell lysates in the future optimization. This would lead to a potentially more robust procedure in biological cryo-EM structural analysis and may extend to the single molecule application or *in situ* ET.

METHODS

Graphene Growth and Transfer. Large single-crystalline graphene membrane with a domain size larger than 3 mm was grown on Cu foil (Alfa-Aesar #46365) via second passivation and multistage carbon supply method reported previously.⁴² No-polymer clean transfer of graphene was conducted with the assistance of isopropanol, within 2 days after graphene synthesis.⁴¹

Fabrication of FGM. First, the as-prepared graphene membrane was oxidized by dropping 7 μ L of reaction reagent mixed of 0.40 M KMnO_4 and 0.20 M NaOH onto the graphene/Au grid, and the reaction was maintained for 50 min. Then, the graphene grid was thoroughly washed by sodium bisulfite solution (1M, Sigma-Aldrich Company) up to 100 min. Subsequently, the graphene grid was modified by mixed solution of 5.0 mM *N*-(3-(dimethylamino)-

propyl)-*N'*-ethylcarbodiimide hydrochloride (EDC, Sigma-Aldrich Company, CAS 25952-53-8), 5.0 mM *N*-hydroxyl-sulfosuccinimide (sulfo-NHS, Sigma-Aldrich Company, CAS 106627-54-7), and 0.10 M MES (Sigma-Aldrich Company) at pH 5.0 for 50 min. Next, the graphene grid was activated by 11.3 mM *N* α ,*N* α -bis(carboxymethyl)-*L*-lysine hydrate (NTA-NH₂, Sigma-Aldrich Company, CAS 941689-36-7) in 50 mM TBE buffer (pH 8.5, Beijinghuaxingbochuang Technology Co. Ltd.) for 2 h, followed by reacting with 11.3 mM NiSO_4 for 1 h. Finally, the modified graphene grid was washed by double-distilled water and used for the subsequent characterizations and protein capture.

Characterization. Aberration-corrected TEM examination was performed using a Thermo Fisher Scientific Vitrobot 80-300 Environmental Titan operated in monochromated mode at 80 kV. Thermo Fisher Scientific Tecnai F30 (acceleration voltage 300 kV) was also used for the low-magnification characterization of the suspended graphene. Water contact-angles were measured using a Dataphysics OCA 20 contact-angle system at room temperature. The morphology of the suspended graphene was characterized using AFM (Bruker dimension icon, scansyst mode, scansyst air tip). The composition characterization was conducted with XPS (Kratos

Analytical AXIS-Ultra with monochromatic Al $K\alpha$ X-ray). Raman spectrum spectroscopy (Horiba, LabRAM HR-800, 633 nm laser wavelength, 100 \times objective) was used to evaluate the crystallinity of the samples.

Biomolecules Purification. N-Terminal His-tagged *Deinococcus radiodurans* PNPase,⁴⁵ N-terminal His-tagged RFP, and C-terminal β subunit His-tagged *Thermoplasma acidophilum* 20S proteasome^{46,47} were purified from *Escherichia coli* cells by following previously reported protocols. Pre-60S ribosomes⁴⁸ were purified from yeast cells according to published methods. Note that, all these purified biological samples were prepared in Ni- or imidazole-free buffer before being used in the experiments.

Negative-Staining EM Analysis of His-Tagged PNPase. A \sim 5 μ L droplet of 100 nM PNPase was applied onto freshly modified graphene grids and incubated for 15 min in a chamber of high humidity at 4 $^{\circ}$ C. Then, the grids were gently washed by sample buffer (20 mM HEPES (pH 7.5), 50 mM NaCl, 1 mM $MgCl_2$) for 3–5 times. Next, 3 μ L of 2% uranyl acetate was pipetted to the grids and allowed to stain for \sim 1 min. After staining, the grids were blotted and air-dried. For imidazole washing experiments, the sample-incubated grids were washed with 300 mM imidazole solution for 5 times, followed by negative staining with 2% uranyl acetate. Negative-staining micrographs were acquired under a Thermo Fisher Scientific Tecnai Spirit 120 electron microscope equipped with a Gatan US4000 CCD camera.

Cryo-EM Experiments and Data Analysis. A \sim 5 μ L droplet of His-tagged 20S proteasomes mixed with pre-60S ribosomes at a molar ratio of \sim 1:1 was pipetted onto grids coated by FGM or NTA modified GM. After 15 min of incubation, the grids were gently washed 3–5 times and then transferred into Thermo Fisher Scientific Vitrobot. The humidity of chamber in Vitrobot was set as 100%, and the temperature was 12 $^{\circ}$ C. After blotting for 2 s at force of -2 , grids were plunge-frozen into liquid ethane and kept in liquid nitrogen. For cryo-specimens in control groups, 3 μ L of protein solution was applied onto freshly glow-discharged continuous-carbon coated grids or holey carbon grids and then blotted by filter paper (Ted Pella, Inc.) in a Thermo Fisher Scientific Vitrobot, followed by plunge-freezing.

Single-particle Cryo-EM data sets in this work were collected on an Thermo Fisher Scientific Tecnai Arctica equipped with an Thermo Fisher Scientific Falcon II direct electron detector camera at an accelerating voltage of 200 kV. Micrographs were acquired at a defocus range of -2.0 to -3.2 μ m with a magnified physical pixel size of 1.27 \AA . The exposure time was set as 1.2 s, and every micrograph was dose-dependently fractionated into 19 frames, at a total accumulated dose of \sim 50 $e/\text{\AA}^2$. For reconstruction of 20S proteasomes on FGM grids, we collected 66 micrographs and used MotionCor2⁴⁹ to correct the beam-induced motion. CTF estimation and defocus values calculation were performed by package CTFIND4,⁵⁰ and the results were manually inspected. A total of 6271 particles were picked, normalized, and iteratively 2D classified by Relion2.1.⁵¹ After discarding particles grouped in poorly defined 2D classes, 6095 particles were left for further reconstruction and refinement. After postprocessing in Relion2.1, we finally got a 3.8 \AA resolution density map estimated by Fourier Shell Correction (FSC) 0.143 cutoff criteria.⁵² For docking of atomic structure, published *T. acidophilum* 20S proteasome (PDB code: 3J9I)⁵³ was fetched from RCSB Protein Data Bank and docked into the 3.8 \AA 3D density map by using fit-in-map operation in UCSF Chimera.⁵⁴ For reconstructions of 20S proteasomes on holey carbon grids or amorphous carbon grids, data sets were collected on the same Thermo Fisher Scientific Tecnai Arctica microscope using setting parameters the same as those on FGM grids. In the data processing, proportions of particles contributed for final reconstructions among the total picked particles were \sim 93% in holey carbon grids and \sim 97% in amorphous carbon grids, respectively.

Cryo-Electron Tomography. Cryo-ET micrographs were acquired on a Thermo Fisher Scientific Titan Krios microscope operated at 300 kV acceleration voltage and equipped with a Gatan K2 camera using SerialEM,⁵⁵ at a dose rate of \sim 3 $e/\text{\AA}^2/\text{s}$ and a total accumulated dose of \sim 100 $e/\text{\AA}^2$. The magnification for data collection

was 64 000 \times , and the calibrated pixel size was 1.772 \AA . For each tilt series, we acquired from $+51$ to -51° with a step of 3° . All tilt series were acquired at a defocus of about -5.0 μ m. MotionCor2⁴⁹ was used to align movie frames (6 frames) in every tilt image. These tilt series were aligned and reconstructed with a binning factor of 4 in IMOD.^{56,57} The 20S proteasome particle position in the cryo-ET density was identified by template matching and visual interpretation.

■ ASSOCIATED CONTENT

📄 Supporting Information

The Supporting Information is available free of charge on the ACS Publications website at DOI: 10.1021/jacs.8b13038.

TEM images of GM, AFM images and XPS survey spectra of GM and FGM, negative-staining EM micrographs of FGM and His-tagged PNPase-loaded FGM, cryo-EM micrograph, FSC curves, and Euler angle distribution of 20S proteasomes (PDF)

■ AUTHOR INFORMATION

Corresponding Authors

*E-mail: yananchen@tsinghua.edu.cn (Y.C.).

*E-mail: hlpeng@pku.edu.cn (H.P.).

*E-mail: hongweiwang@tsinghua.edu.cn (H.W.).

ORCID

Zhongfan Liu: 0000-0003-0065-7988

Hailin Peng: 0000-0003-1569-0238

Hong-Wei Wang: 0000-0001-9494-8780

Author Contributions

[▽]N.L., J.C.Z., and Y.N.C. contributed equally to this work.

Notes

The authors declare no competing financial interest.

■ ACKNOWLEDGMENTS

We are thankful to Li Lin for the graphene preparation at the initial stage, and we thank Xiao Fan, Jia Wang, and Lingyun Zhao of the Wang Lab for their helpful suggestions on cryo-data processing. We thank Meng Yin in Xueming Li lab (Tsinghua University) for providing 20S proteasome sample and Dr. Chengying Ma in Ning Gao lab (Peking University) for providing 60S ribosome sample. We also thank Jianlin Lei, Lingpeng Cheng, Xiaomin Li, Xiaomei Li, Xiaofeng Hu, and Danyang Li at the Tsinghua University Branch of the China National Center for Protein Sciences (Beijing) for providing technical support in electron microscopy operation and data collection. The authors acknowledge Electron Microscopy Laboratory in Peking University for the use of Cs-corrected electron microscope. This work is supported by grant 2016YFA0501100 (to H.-W.W.) from the Ministry of Science and Technology of China and grant Z161100000116034 (to H.-W.W.) from the Beijing Municipal Science & Technology Commission. The work of J.C.Z. and H.L.P. was supported by the National Natural Science Foundation of China (21525310) and the National Basic Research Program of China (2014CB932500 and 2016YFA0200101). Y.N.C. acknowledges the China Postdoctoral Science Foundation (2017M610079, 2018T110090) for financial support.

■ REFERENCES

(1) Bai, X.; McMullan, G.; Scheres, S. H. W. How Cryo-EM Is Revolutionizing Structural Biology. *Trends Biochem. Sci.* **2015**, *40* (1), 49–57.

- (2) Cheng, Y. Single-Particle Cryo-EM at Crystallographic Resolution. *Cell* **2015**, *161* (3), 450–457.
- (3) Jain, T.; Sheehan, P.; Crum, J.; Carragher, B.; Potter, C. S. Spotiton: A Prototype for an Integrated Inkjet Dispense and Vitrification System for Cryo-TEM. *J. Struct. Biol.* **2012**, *179* (1), 68–75.
- (4) Feng, X.; Fu, Z.; Kaledhonkar, S.; Jia, Y.; Shah, B.; Jin, A.; Liu, Z.; Sun, M.; Chen, B.; Grassucci, R. A.; et al. A Fast and Effective Microfluidic Spraying-Plunging Method for High-Resolution Single-Particle Cryo-EM. *Structure* **2017**, *25* (4), 663–670.e3.
- (5) Arnold, S. A.; Albiez, S.; Bieri, A.; Syntychaki, A.; Adaxo, R.; McLeod, R. A.; Goldie, K. N.; Stahlberg, H.; Braun, T. Blotting-Free and Lossless Cryo-Electron Microscopy Grid Preparation from Nanoliter-Sized Protein Samples and Single-Cell Extracts. *J. Struct. Biol.* **2017**, *197* (3), 220–226.
- (6) Adrian, M.; Dubochet, J.; Lepault, J.; McDowell, A. W. Cryo-Electron Microscopy of Viruses. *Nature* **1984**, *308* (5954), 32–36.
- (7) Snijder, J.; Borst, A. J.; Dosey, A.; Walls, A. C.; Burrell, A.; Reddy, V. S.; Kollman, J. M.; Velesler, D. Vitrification after Multiple Rounds of Sample Application and Blotting Improves Particle Density on Cryo-Electron Microscopy Grids. *J. Struct. Biol.* **2017**, *198* (1), 38–42.
- (8) Zhao, M.; Wu, S.; Zhou, Q.; Vivona, S.; Cipriano, D. J.; Cheng, Y.; Brunger, A. T. Mechanistic Insights into the Recycling Machine of the SNARE Complex. *Nature* **2015**, *518* (7537), 61–67.
- (9) Glaeser, R. M. Proteins, Interfaces, and Cryo-EM Grids. *Curr. Opin. Colloid Interface Sci.* **2018**, *34*, 1–8.
- (10) Glaeser, R. M.; Han, B.-G. Opinion: Hazards Faced by Macromolecules When Confined to Thin Aqueous Films. *Biophys. Rep.* **2017**, *3* (1–3), 1–7.
- (11) Noble, A. J.; Wei, H.; Dandey, V. P.; Zhang, Z.; Tan, Y. Z.; Potter, C. S.; Carragher, B. Reducing Effects of Particle Adsorption to the Air–water Interface in Cryo-EM. *Nat. Methods* **2018**, *15* (10), 793.
- (12) Gao, H.; Zhou, Z.; Rawat, U.; Huang, C.; Bouakaz, L.; Wang, C.; Cheng, Z.; Liu, Y.; Zavalov, A.; Gursky, R.; et al. RF3 Induces Ribosomal Conformational Changes Responsible for Dissociation of Class I Release Factors. *Cell* **2007**, *129* (5), 929–941.
- (13) Grassucci, R. A.; Taylor, D. J.; Frank, J. Preparation of Macromolecular Complexes for Cryo-Electron Microscopy. *Nat. Protoc.* **2007**, *2* (12), 3239–3246.
- (14) Wang, L.; Ounjai, P.; Sigworth, F. J. Streptavidin Crystals as Nanostructured Supports and Image-Calibration References for Cryo-EM Data Collection. *J. Struct. Biol.* **2008**, *164* (2), 190–198.
- (15) Han, B.-G.; Watson, Z.; Cate, J. H. D.; Glaeser, R. M. Monolayer-Crystal Streptavidin Support Films Provide an Internal Standard of Cryo-EM Image Quality. *J. Struct. Biol.* **2017**, *200* (3), 307–313.
- (16) Kelly, D. F.; Dukovski, D.; Walz, T. Strategy for the Use of Affinity Grids to Prepare Non-His-Tagged Macromolecular Complexes for Single-Particle Electron Microscopy. *J. Mol. Biol.* **2010**, *400* (4), 675–681.
- (17) Kelly, D. F.; Dukovski, D.; Walz, T. Monolayer Purification: A Rapid Method for Isolating Protein Complexes for Single-Particle Electron Microscopy. *Proc. Natl. Acad. Sci. U. S. A.* **2008**, *105* (12), 4703–4708.
- (18) Selmi, D. N.; Adamson, R. J.; Attrill, H.; Goddard, A. D.; Gilbert, R. J. C.; Watts, A.; Turberfield, A. J. DNA-Templated Protein Arrays for Single-Molecule Imaging. *Nano Lett.* **2011**, *11* (2), 657–660.
- (19) Llaguno, M. C.; Xu, H.; Shi, L.; Huang, N.; Zhang, H.; Liu, Q.; Jiang, Q.-X. Chemically Functionalized Carbon Films for Single Molecule Imaging. *J. Struct. Biol.* **2014**, *185* (3), 405–417.
- (20) Geim, A. K.; Novoselov, K. S. The Rise of Graphene. *Nat. Mater.* **2007**, *6* (3), 183–191.
- (21) Balandin, A. A.; Ghosh, S.; Bao, W.; Calizo, I.; Teweldebrhan, D.; Miao, F.; Lau, C. N. Superior Thermal Conductivity of Single-Layer Graphene. *Nano Lett.* **2008**, *8* (3), 902–907.
- (22) Wang, Y.; Chen, Y.; Lacey, S. D.; Xu, L.; Xie, H.; Li, T.; Danner, V. A.; Hu, L. Reduced Graphene Oxide Film with Record-High Conductivity and Mobility. *Mater. Today* **2018**, *21* (2), 186–192.
- (23) Chen, Y.; Fu, K.; Zhu, S.; Luo, W.; Wang, Y.; Li, Y.; Hitz, E.; Yao, Y.; Dai, J.; Wan, J.; et al. Reduced Graphene Oxide Films with Ultrahigh Conductivity as Li-Ion Battery Current Collectors. *Nano Lett.* **2016**, *16* (6), 3616–3623.
- (24) Bao, W.; Pickel, A. D.; Zhang, Q.; Chen, Y.; Yao, Y.; Wan, J.; Fu, K.; Wang, Y.; Dai, J.; Zhu, H.; et al. Flexible, High Temperature, Planar Lighting with Large Scale Printable Nanocarbon Paper. *Adv. Mater.* **2016**, *28* (23), 4684–4691.
- (25) Wang, B.; Cunnings, B. V.; Park, S.-Y.; Huang, M.; Kim, J.-Y.; Ruoff, R. S. Graphene Coatings as Barrier Layers to Prevent the Water-Induced Corrosion of Silicate Glass. *ACS Nano* **2016**, *10* (11), 9794–9800.
- (26) Chen, Y.; Egan, G. C.; Wan, J.; Zhu, S.; Jacob, R. J.; Zhou, W.; Dai, J.; Wang, Y.; Danner, V. A.; Yao, Y.; et al. Ultra-Fast Self-Assembly and Stabilization of Reactive Nanoparticles in Reduced Graphene Oxide Films. *Nat. Commun.* **2016**, *7*, 12332.
- (27) Lee, C.; Wei, X.; Kysar, J. W.; Hone, J. Measurement of the Elastic Properties and Intrinsic Strength of Monolayer Graphene. *Science* **2008**, *321* (5887), 385–388.
- (28) Wang, C.; Qiao, Q.; Shokuhfar, T.; Klie, R. F. High-Resolution Electron Microscopy and Spectroscopy of Ferritin in Biocompatible Graphene Liquid Cells and Graphene Sandwiches. *Adv. Mater.* **2014**, *26* (21), 3410–3414.
- (29) Bai, Y.; Ming, Z.; Cao, Y.; Feng, S.; Yang, H.; Chen, L.; Yang, S.-T. Influence of Graphene Oxide and Reduced Graphene Oxide on the Activity and Conformation of Lysozyme. *Colloids Surf., B* **2017**, *154*, 96–103.
- (30) Li, D.; Müller, M. B.; Gilje, S.; Kaner, R. B.; Wallace, G. G. Processable Aqueous Dispersions of Graphene Nanosheets. *Nat. Nanotechnol.* **2008**, *3* (2), 101–105.
- (31) Pantelic, R. S.; Meyer, J. C.; Kaiser, U.; Baumeister, W.; Plitzko, J. M. Graphene Oxide: A Substrate for Optimizing Preparations of Frozen-Hydrated Samples. *J. Struct. Biol.* **2010**, *170* (1), 152–156.
- (32) Palovcak, E.; Wang, F.; Zheng, S. Q.; Yu, Z.; Li, S.; Betegon, M.; Bulkeley, D.; Agard, D. A.; Cheng, Y. A Simple and Robust Procedure for Preparing Graphene-Oxide Cryo-EM Grids. *J. Struct. Biol.* **2018**, *204* (1), 80–84.
- (33) Pantelic, R. S.; Suk, J. W.; Hao, Y.; Ruoff, R. S.; Stahlberg, H. Oxidative Doping Renders Graphene Hydrophilic, Facilitating Its Use As a Support in Biological TEM. *Nano Lett.* **2011**, *11* (10), 4319–4323.
- (34) Pantelic, R. S.; Fu, W.; Schönenberger, C.; Stahlberg, H. Rendering Graphene Supports Hydrophilic with Non-Covalent Aromatic Functionalization for Transmission Electron Microscopy. *Appl. Phys. Lett.* **2014**, *104* (13), 134103–134107.
- (35) Russo, C. J.; Passmore, L. A. Controlling Protein Adsorption on Graphene for Cryo-EM Using Low-Energy Hydrogen Plasmas. *Nat. Methods* **2014**, *11* (6), 649–652.
- (36) Llaguno, M. C.; Xu, H.; Shi, L.; Huang, N.; Zhang, H.; Liu, Q.; Jiang, Q.-X. Chemically Functionalized Carbon Films for Single Molecule Imaging. *J. Struct. Biol.* **2014**, *185* (3), 405–417.
- (37) Yu, G.; Li, K.; Jiang, W. Antibody-Based Affinity Cryo-EM Grid. *Methods* **2016**, *100*, 16–24.
- (38) Kelly, D. F.; Abeyrathne, P. D.; Dukovski, D.; Walz, T. The Affinity Grid: A Pre-Fabricated EM Grid for Monolayer Purification. *J. Mol. Biol.* **2008**, *382* (2), 423–433.
- (39) Kelly, D. F.; Dukovski, D.; Walz, T. Strategy for the Use of Affinity Grids to Prepare Non-His-Tagged Macromolecular Complexes for Single-Particle Electron Microscopy. *J. Mol. Biol.* **2010**, *400* (4), 675–681.
- (40) Benjamin, C. J.; Wright, K. J.; Bolton, S. C.; Hyun, S.-H.; Krynski, K.; Grover, M.; Yu, G.; Guo, F.; Kinzer-Ursem, T. L.; Jiang, W.; et al. Selective Capture of Histidine-Tagged Proteins from Cell Lysates Using TEM Grids Modified with NTA-Graphene Oxide. *Sci. Rep.* **2016**, *6*, 32500.

(41) Zhang, J.; Lin, L.; Sun, L.; Huang, Y.; Koh, A. L.; Dang, W.; Yin, J.; Wang, M.; Tan, C.; Li, T.; et al. Clean Transfer of Large Graphene Single Crystals for High-Intactness Suspended Membranes and Liquid Cells. *Adv. Mater.* **2017**, *29* (26), 1700639.

(42) Lin, L.; Sun, L.; Zhang, J.; Sun, J.; Koh, A. L.; Peng, H.; Liu, Z. Rapid Growth of Large Single-Crystalline Graphene via Second Passivation and Multistage Carbon Supply. *Adv. Mater.* **2016**, *28* (23), 4671–4677.

(43) Dong, C.; Guo, L.; He, Y.; Chen, C.; Qian, Y.; Chen, Y.; Xu, L. Sandwich-like Ni₂P Nanoarray/nitrogen-Doped Graphene Nano-architecture as a High-Performance Anode for Sodium and Lithium Ion Batteries. *Energy Storage Mater.* **2018**, *15*, 234–241.

(44) Taylor, K. A.; Glaeser, R. M. Retrospective on the Early Development of Cryoelectron Microscopy of Macromolecules and a Prospective on Opportunities for the Future. *J. Struct. Biol.* **2008**, *163* (3), 214–223.

(45) Chen, X.; Taylor, D. W.; Fowler, C. C.; Galan, J. E.; Wang, H.-W.; Wolin, S. L. An RNA Degradation Machine Sculpted by Ro Autoantigen and Noncoding RNA. *Cell* **2013**, *153* (1), 166–177.

(46) Yu, Y.; Smith, D. M.; Kim, H. M.; Rodriguez, V.; Goldberg, A. L.; Cheng, Y. Interactions of PAN's C termini with Archaeal 20S Proteasome and Implications for the Eukaryotic proteasome–ATPase Interactions. *EMBO J.* **2010**, *29* (3), 692–702.

(47) Rabl, J.; Smith, D. M.; Yu, Y.; Chang, S.-C.; Goldberg, A. L.; Cheng, Y. Mechanism of Gate Opening in the 20S Proteasome by the Proteasomal ATPases. *Mol. Cell* **2008**, *30* (3), 360–368.

(48) Ma, C.; Wu, S.; Li, N.; Chen, Y.; Yan, K.; Li, Z.; Zheng, L.; Lei, J.; Woolford, J. L., Jr.; Gao, N. Structural Snapshot of Cytoplasmic Pre-60S Ribosomal Particles Bound by Nmd3, Lsg1, Tif6 and Reh1. *Nat. Struct. Mol. Biol.* **2017**, *24* (3), 214–220.

(49) Zheng, S. Q.; Palovcak, E.; Armache, J.-P.; Verba, K. A.; Cheng, Y.; Agard, D. A. MotionCor2: Anisotropic Correction of Beam-Induced Motion for Improved Cryo-Electron Microscopy. *Nat. Methods* **2017**, *14* (4), 331–332.

(50) Rohou, A.; Grigorieff, N. CTFFIND4: Fast and Accurate Defocus Estimation from Electron Micrographs. *J. Struct. Biol.* **2015**, *192* (2), 216–221.

(51) Scheres, S. H. W. RELION: Implementation of a Bayesian Approach to Cryo-EM Structure Determination. *J. Struct. Biol.* **2012**, *180* (3), 519–530.

(52) Rosenthal, P. B.; Henderson, R. Optimal Determination of Particle Orientation, Absolute Hand, and Contrast Loss in Single-Particle Electron Cryomicroscopy. *J. Mol. Biol.* **2003**, *333* (4), 721–745.

(53) Li, X.; Mooney, P.; Zheng, S.; Booth, C. R.; Braunfeld, M. B.; Gubbens, S.; Agard, D. A.; Cheng, Y. Electron Counting and Beam-Induced Motion Correction Enable near-Atomic-Resolution Single-Particle Cryo-EM. *Nat. Methods* **2013**, *10* (6), 584–590.

(54) Pettersen, E. F.; Goddard, T. D.; Huang, C. C.; Couch, G. S.; Greenblatt, D. M.; Meng, E. C.; Ferrin, T. E. UCSF Chimera—a Visualization System for Exploratory Research and Analysis. *J. Comput. Chem.* **2004**, *25* (13), 1605–1612.

(55) Mastronarde, D. N. Automated Electron Microscope Tomography Using Robust Prediction of Specimen Movements. *J. Struct. Biol.* **2005**, *152* (1), 36–51.

(56) Kremer, J. R.; Mastronarde, D. N.; McIntosh, J. R. Computer Visualization of Three-Dimensional Image Data Using IMOD. *J. Struct. Biol.* **1996**, *116* (1), 71–76.

(57) Mastronarde, D. N. Dual-Axis Tomography: An Approach with Alignment Methods That Preserve Resolution. *J. Struct. Biol.* **1997**, *120* (3), 343–352.